PCCP

ROYAL SOCIETY OF CHEMISTRY

PAPER

View Article Online
View Journal

Cite this: DOI: 10.1039/d3cp01413d

A theoretical characterization method for non-spherical core–shell nanoparticles by XPS†

J. M. Gong,[acd] M. S. S. Khan,[e] B. Da,*[c] H. Yoshikawa,[c] S. Tanuma[d] and Z. J. Ding *[ab]

Received 28th March 2023,
Accepted 20th May 2023

DOI: 10.1039/d3cp01413d

rsc.li/pccp

Core–shell nanoparticles (NPs) are active research areas for their unique properties and wide applications. By changing the elemental composition in the core and shell, a series of core–shell NPs with specific functions can be obtained, where the sizes of the core and shell also influence the properties. X-ray photoelectron spectroscopy (XPS) is useful in this context as a means of quantitatively analyzing such NPs. The empirical formula proposed by Shard [*J. Phys. Chem. C*, 2012, **116**(31), 16806–16813] for calculating the shell thickness of the spherical core–shell NPs has been verified by Powell *et al.* [*J. Phys. Chem. C*, 2016, **120**(39), 22730–22738] through a simulation of XPS with Simulation of Electron Spectra for Surface Analysis (SESSA) software. However, real core–shell NPs are not necessarily ideal spheres; such NPs can have rich shapes and uneven thicknesses. This work aims to extend the Shard formula to non-ideal core–shell NPs. We have used a Monte Carlo simulation method to study the XPS signal variation with the shell thickness for several modeled non-spherical shapes of core–shell NPs including some complex geometric structures which are numerically constructed with finite-element triangular meshes. Five types of non-spherical shapes, *i.e.* egg, ellipsoid, rod, rough-surface, and star shapes, are considered, while the size parameters are varied over a wide range. The equivalent radius and equivalent thickness are defined to characterize the average size of the nanoparticles for the use of the Shard formula. We have thus derived an extended Shard formula for the specific core–shell NPs, with which the relative error between the predicted shell thickness and the real thickness can be reduced to less than 10%.

Introduction

Nanoparticles (NPs), for their high specific surface area, stability, and special surface properties exhibited by the nanoscale size,[1,2] have unique physical properties quite different from their counterpart bulk materials. On the nanometer scale there are many size-dependent properties—such as, quantum bonding (semiconductor NPs), plasmon resonance (metal NPs), and superparamagnetism (magnetic NPs). Such characteristics render NPs highly functional. In the NP family, the core–shell nanostructure is a valuable entity, which can impart higher thermal and chemical stability, lower toxicity, and better permeability to specific target cells compared with other NPs.[3] In the late 1980s and early 1990s, researchers discovered that multilayer composite semiconductor NPs had enhanced efficiency and even new properties, and consequently the core–shell concept became well-established.[4–9] Currently, the study of core–shell NPs is an active area of research and NPs have found many applications in chemistry, catalysis, biology, electricity, optics, medicine, and many other fields.[10]

For comprehensive NP analysis, different characterization techniques are necessary. Commonly used techniques include dynamic light scattering, disc centrifugation, nanoparticle tracking analysis, tunable resistive pulse sensing,[11] atomic force microscopy (AFM),[12] scanning electron microscopy (SEM), transmission electron microscopy (TEM), thermogravimetric analysis,[13] X-ray photoelectron spectroscopy (XPS), photoluminescence and ultraviolet-visible spectroscopy, *etc.* Since the size of NPs has a crucial influence on their properties, accurate size measurement is a chief concern in almost all fields of NP applications. Dynamic light scattering and NP tracking analysis can only be applied to ensemble-level NPs, while other

[a] *Department of Physics, University of Science and Technology of China, Hefei, Anhui 230026, P. R. China. E-mail: zjding@ustc.edu.cn*
[b] *Hefei National Research Center for Physical Sciences at the Microscale, University of Science and Technology of China, Hefei, Anhui 230026, P. R. China*
[c] *Center for Basic Research on Materials, National Institute for Materials Science, Tsukuba, Ibaraki 305-0044, Japan. E-mail: DA.Bo@nims.go.jp*
[d] *Materials Data Platform Center, National Institute for Materials Science, 1-1 Namiki, Tsukuba, Ibaraki 305-0044, Japan*
[e] *Key Laboratory of Materials Physics, Institute of Solid State Physics, Chinese Academy of Sciences, Hefei, Anhui 230031, People's Republic of China*

† Electronic supplementary information (ESI) available. See DOI: https://doi.org/10.1039/d3cp01413d

techniques are compatible with single-NP analysis. Thermogravimetric analysis can be used to determine the quantity of coating on the surface of metal NPs.[13] Tunable resistive pulse sensing can measure the radius of NPs but cannot measure the shell thickness of core–shell NPs in detail. Furthermore, the operation of AFM is complex; and regarding soft or small-sized NPs, the shape may substantially change from the influence of the AFM cutting-edge force. In addition, when processing AFM images, the choice of algorithms considerably influences the results, which imparts difficulties in obtaining accurate information.[14] Electron microscopy methods like SEM and TEM can cause significant radiation damage to the material.

In comparison, XPS is an efficient, convenient, and low-cost measurement spectroscopic technique, which is widely being used to characterize the chemical properties and composition of NPs.[15,16] Meanwhile, XPS can also provide certain material size information with very little damage compared to electron beam methods. Conventional methods for obtaining the thickness of the overlayer-film material are based on the exponential attenuation approximation for the photoelectron intensity.[17,18] However, it is generally difficult to quantitatively measure the shell thickness of core–shell NPs because the signal transport process in the nanostructure is very complicated, while the accurate measurement of the size of the NPs is essential for most applications.

Baer and Engelhard discussed the impact of nanostructures on XPS data and the related challenges of understanding nanostructured materials.[19] Davis proposed a method to estimate the mean particle size of metal NPs by using the ratio of the intensities of two photoemission lines (or Auger lines)[20] and several studies that used Davis's model have yielded satisfactory estimations of NP size.[21–24] Yang *et al.* proposed a method for calculating the average size of spherical clusters on a surface, by using XPS emission intensity ratios.[25] Recently, Shard proposed an empirical formula that uses XPS data to measure the shell thickness of core–shell NPs.[26] Subsequently, Powell *et al.* applied this formula to simulations with ideal core–shell NPs, where both the spherical core and shell were considered and the shell thickness was taken uniform. They first considered the case that the core and shell were made of the same material, Cu, while the signals were Cu $2p_{3/2}$ photoelectrons excited by Al Kα X-rays and found the formula to be quite satisfactory for determining the shell thickness.[27] The Shard formula was also applied to the case of different core–shell materials and the derived shell thicknesses agreed well with the assumed values in their simulations.[28]

The aforementioned breakthrough in developing and experimentally validating the Shard formula facilitates the measurement of the shell thickness of core–shell NPs by XPS. However, it is worth noting that the current Shard formula can only be applied to ideal spherical NPs. With the development of controlled synthesis technologies, researchers can now design various core–shell NP structures in order to obtain different properties and functions.[29,30] Therefore, core–shell NPs are no longer just in simple sphere shapes, but many different morphological shapes, such as ellipsoids, rods, and stars, are now available. Quantitative measurement of the size of these NPs has increasingly become the focus of attention. In the present work, we extend the Shard formula to non-spherical core–shell NPs and thus obtain the shell thickness (equivalent thickness) with a Monte Carlo electron trajectory simulation method, which can provide a reference for the measurements of the shell thickness of other real core–shell NPs.

In this context, a Monte Carlo simulation approach is pertinent. Monte Carlo methods have been extensively employed over recent decades to simulate the interactions between electrons and solids for signal analysis in electron microscopy and electron spectroscopy.[31–36] Simulation results were found to be in good agreement with experiments.[37–42] By combining Mott's cross section for describing the electron elastic scattering and the dielectric function for the electron inelastic scattering, we have developed and applied classic trajectory Monte Carlo (CTMC) simulation models to SEM,[43–52] AES[53–56] and reflected electron energy loss spectroscopy[57–64] with different simulation codes.[65] This CTMC simulation approach has also been applied to the analysis of thin film nanomaterials.[66–68] Even though one of the most significant advantages of the MC simulation method is on easy handling of complex sample geometrical boundaries, the previous Monte Carlo simulations have been mostly performed for simple and regular sample geometries until the applications of various numerical methods to the construction of the material interfaces.[47,49,51,52,69–74] For our present purpose it is necessary to apply these geometry construction methods to real-world nanomaterial morphologies for more comprehensive XPS analyses. Powell *et al.* have used the simulation of electron spectra for surface analysis (SESSA) software,[27,28] where the sample structure was created with the PENGEOM geometry package, which uses analytic quadric surfaces to construct a NP morphology.[75] The PENGEOM package has also been implemented in some Monte Carlo simulators like PENELOPE.[76,77] The complex geometry construction may also be achieved by the combination of the basic shapes (*e.g.*, spheres, cylinders, blocks *etc.*) using the Boolean operations (*e.g.*, union, intersection, difference, *etc.*).[44,69,78]

Here we will use the finite element method which is a more general method for the construction of an arbitrary complex structure and interface morphology.[49,74] The finite-element triangular-gridding method is versatile for approximately describing many real objects, such as an irregular rough surface. We consider here five core–shell nanostructures with different chemical elements in the core and the shell and derive an extended Shard formula for the shell thickness measurement. Among the five shapes we present, the formulae for the rod and star shapes seem to not depend on the degree of deformation, whereas the corrected formulae for the ellipsoid, egg, and rough surface shapes do depend on the degree of deformation.

Theoretical methods

Monte Carlo model

In a Monte Carlo simulation, the transport process of signal electrons in materials consists of electron elastic and inelastic

scattering events, which are randomly sampled with respective scattering cross-sections. An up-to-date classical trajectory Monte Carlo approach is applied in the present work for simulating electron–solid interactions. To describe electron elastic scattering, we have used the Mott's cross-section[79] combined with Thomas-Fermi-Dirac potential[80] for the interaction of a kinetic electron with an atom. The expression of the differential elastic scattering cross-section considering the relativistic effect is as follows:

$$\frac{d\sigma_e}{d\Omega} = |f(\theta)|^2 + |g(\theta)|^2 \quad (1)$$

where θ is the scattering angle, $f(\theta)$ and $g(\theta)$ are the spin-up and spin-down scattering amplitudes:

$$f(\theta) = \frac{1}{2iK}\sum_l \{(l+1)[\exp(2i\delta_l^+) - 1] + l[\exp(2i\delta_l^-) - 1]\} P_l(\cos\theta); \quad (2)$$

$$g(\theta) = \frac{1}{2iK}\sum_l [\exp(2i\delta_l^-) - \exp(2i\delta_l^+)] P_l^1(\cos\theta), \quad (3)$$

where $\hbar K$ is the momentum of the scattering electron, $P_l(\cos\theta)$ and $P_l^1(\cos\theta)$ are the Legendre and the first-order associated Legendre functions, respectively; δ_l^+ and δ_l^- are spin-up and spin-down phase shifts of the lth partial wave, respectively. The solution of the Dirac equation for the interaction of the electron and the atomic potential $V(r)$ leads to the following expression of the phase shifts:

$$\tan\delta_l^{\pm} = \frac{Kj_{l+1}(Kr) - j_l(Kr)\left\{\frac{1}{c}\left(E - V(r) + c^2\right)\tan\phi_l^{\pm}(r) + \frac{1}{r}(1 + l + \kappa^{\pm})\right\}}{Kn_{l+1}(Kr) - n_l(Kr)\left\{\frac{1}{c}\left(E - V(r) + c^2\right)\tan\phi_l^{\pm}(r) + \frac{1}{r}(1 + l + \kappa^{\pm})\right\}}, \quad (4)$$

where $j_l(Kr)$ and $n_l(Kr)$ are spherical Bessel and Neumann functions, respectively. The phase shift for each lth partial wave can be obtained as long as the value of $\phi(r_{max})$ is known, where r_{max} is a large value of r such that $V(r_{max}) \simeq 0$. Because eqn (4) is derived from the limit case of $V(r) \simeq 0$. The TFD potential has a finite maximum radius, so eqn (4) can be estimated from this radius. Fig. 1 shows the electron differential elastic scattering cross sections calculated for C and Au atoms at some electron kinetic energies. There are several specific peaks/valleys for heavy elements at low electron energies (*e.g.* Au here), which indicate greater/smaller scattering probabilities at corresponding angles.

Dielectric functional approach is employed to describe electron inelastic scattering in a condensed medium. The double differential cross section of inelastic scattering is given as follows:

$$\frac{d^2\lambda_{in}^{-1}}{d(\hbar\omega)dq} = \frac{1}{\pi a_0 E}\mathrm{Im}\left\{\frac{-1}{\varepsilon(q,\omega)}\right\}\frac{1}{q}, \quad (5)$$

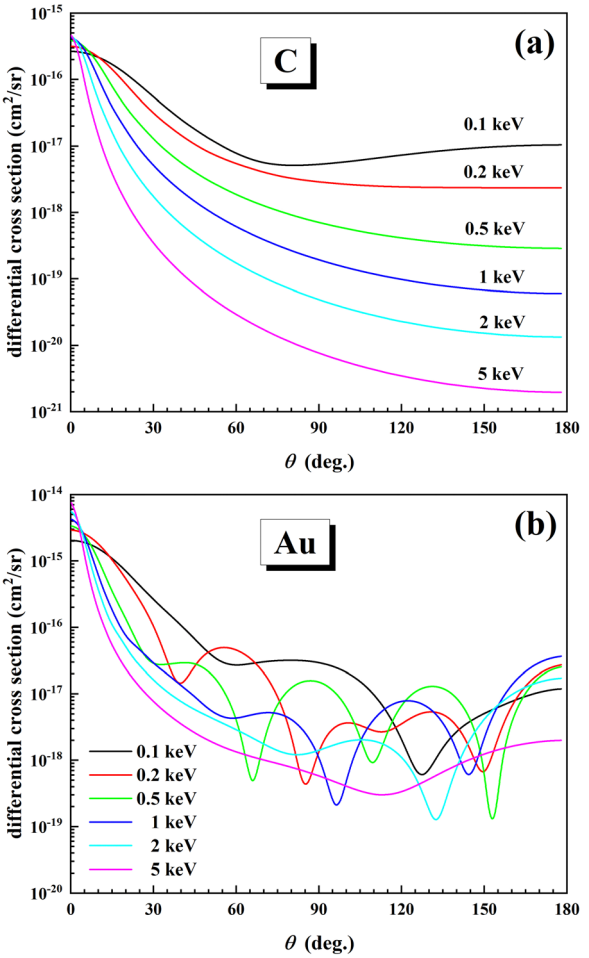

Fig. 1 Differential elastic scattering cross sections for electrons interaction with atoms of: (a) carbon; (b) gold.

where λ_{in} is electron inelastic mean free path (IMFP), $\hbar q$ is momentum transfer and $\Delta E = \hbar\omega$ is the energy loss from an electron of kinetic energy $E = (\hbar K)^2/2m$ to the material described by the dielectric function of $\varepsilon(q,\omega)$. a_0 is the Bohr radius and $\hbar$ is the reduced Planck constant.

The experimental data of optical dielectric function, $\varepsilon(\omega)$, compiled in a database[81] were used to derive the q-dependent energy loss function (ELF), $\mathrm{Im}\{-1/\varepsilon(q,\omega)\}$, with the full Penn algorithm (FPA),[82,83] where we have assumed that the electronic transition in a nanostructure is the same as that in the bulk state. Since the momentum transfer is related to the scattering angle, by a variable change the double differential inelastic scattering cross section in eqn (5) is rewritten as,

$$\frac{d^2\lambda_{in}^{-1}}{d(\Delta E)d\Omega} = \frac{\hbar}{(\pi a_0 e)^2 E}\mathrm{Im}\left\{\frac{-1}{\varepsilon(q,\omega)}\right\}\frac{1}{q^2}\sqrt{E(E-\Delta E)}. \quad (6)$$

The differential inelastic cross section in energy loss can then be obtained from integration over the solid angles, through which the specific energy loss as well as the scattering angle can be randomly sampled in a Monte Carlo simulation.[34] Fig. 2

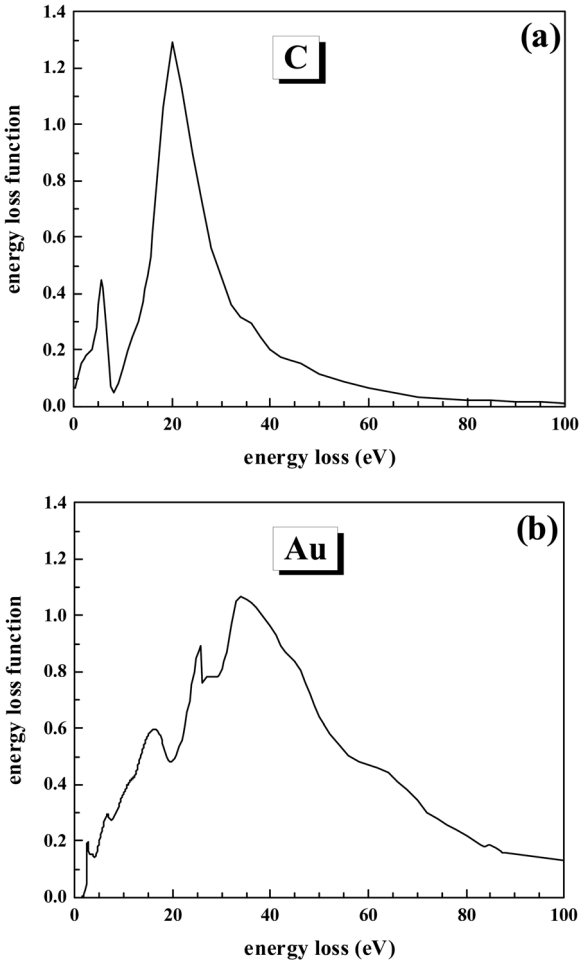

Fig. 2 The optical energy loss functions of amorphous carbon and gold.[81,84]

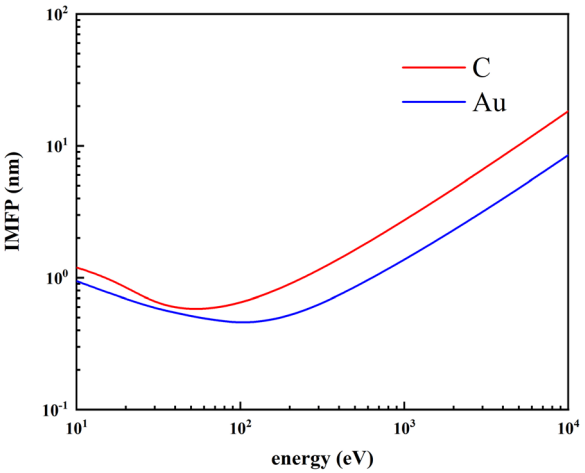

Fig. 3 The inelastic mean free path derived from FPA model for carbon and gold.

illustrates the ELFs of bulk amorphous carbon and gold used in the simulation. Fig. 3 shows the calculated IMFPs for C and Au.

In our Monte Carlo simulation of the photoelectron transportation process, the excitation sites of the photoelectrons are assumed to be homogeneously distributed within a core–shell NP considering the large spot size of an incident X-ray. Fig. 4 shows examples of simulated electron trajectories travelling in a sphere or rod shape C-core/Au-shell NP, where the trajectories are made of the connected spatial positions of Monte Carlo sampled electron scattering events. In Fig. 4, for the sake of visual clarity, the birth positions of the photoelectrons are all set at the center of a NP. It is seen that most of the excited core photoelectrons cannot escape from the shell to be detected for such core and shell sizes; therefore, only those photoelectrons excited far from the center will be more likely to be the detected signals.

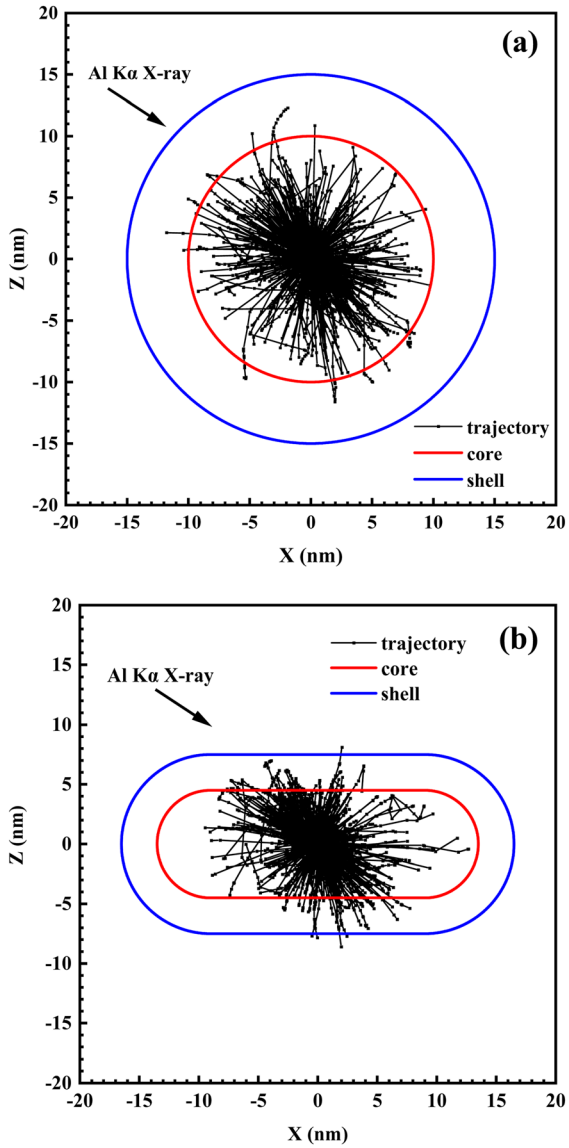

Fig. 4 Projection of 1000 electron trajectories of C 1s photoelectron signals (284.4 eV) travelling in a C-core/Au-shell NP, where the birth position of these electrons is set at the center of a NP. Electron trajectories are terminated when an inelastic scattering event has happened inside the core–shell NP. The red and blue lines indicate the core and shell surface respectively. (a) sphere NP; (b) rod NP.

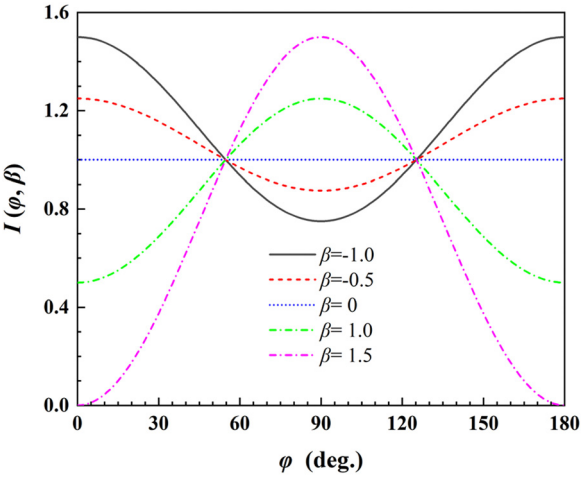

Fig. 5 Photoelectron excitation probability distribution I as a function of emission angle φ and the asymmetry parameter β.

In addition, photoelectrons are generated in an asymmetrical angular distribution (Fig. 5) about the incident X-ray direction according to the following relation,[85]

$$I(\varphi, \beta) = 1 - \frac{\beta}{4}(3\cos^2\varphi - 1), \quad (7)$$

where φ is the angle between the directions of incident X-ray and of excited photoelectron, and β is the asymmetry parameter whose value depends on the type of element, subshell and energy of the photoelectrons (and of course on the excitation light source); it is given as β = 2.0 for C 1s photoelectrons and β = 1.04 for Au $4f_{7/2}$ photoelectrons excited by Al-Kα X-rays.[86]

Finite element method

Distinct from use of the quadric surface method of the PENGEOM software package in SESSA to construct complex configurations,[75] a finite-element triangular mesh was used in the present work to construct the interface of complex structures. The meshing of the NP interfaces in the present work was all produced with Gmesh. Gmesh is an open-source and straightforward three-dimensional finite-element mesh generator,[87] with which the grid sizes produced are essentially the same and can be read in a variety of formats. Fig. 6 shows the mesh for typically spherical core–shell NPs, where the core and shell are both spheres and the shell thickness is uniform. Yet in the present work five typical irregular NPs are considered; they are egg-, ellipsoid-, rod-, rough-surface,

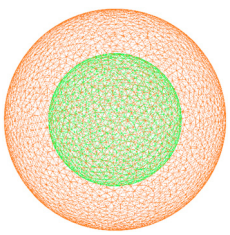

Fig. 6 Schematic of a spherical core–shell structure constructed with a finite-element triangle mesh.

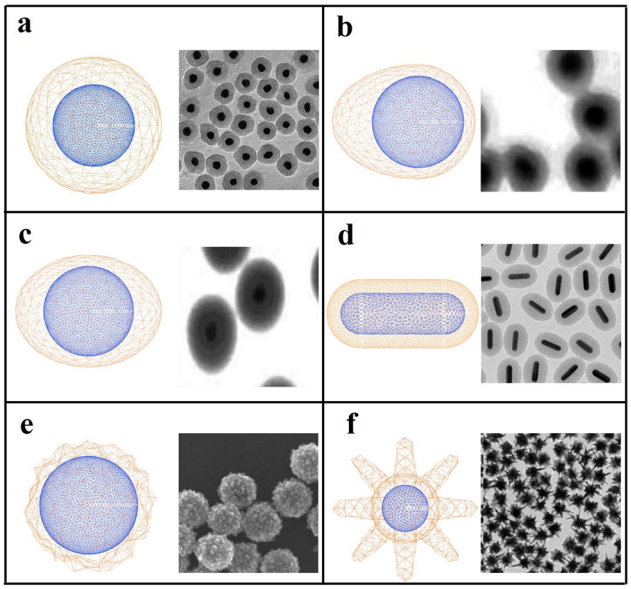

Fig. 7 Schematic of core–shell NP shapes in experiments: (a) sphere;[88] (b) egg-shaped;[89] (c) ellipsoid-shaped;[89] (d) rod-shaped;[90] (e) rough surface;[91] (f) star-shaped.[90]

and star-shaped core–shell NPs, as shown by Fig. 7. The size of the NPs considered is in the order of 10 nm. Furthermore, we have considered the deformation of the NPs gradually changing from ideal central spheres to a morphology of the considered structure as illustrated in Fig. 8. Regarding the egg-shaped core–shell NPs in Fig. 8(b.1)–(b.6), a semi-ellipsoid and hemisphere were combined to form a shell. In this context, the core sphere and shell hemisphere have an identical center. For the other four shapes, the core and shell also have the same center position. Tables 1.1–1.5 in Appendix I show the characteristic parameters of each kind of NP. In the present work, we first apply the Shard formula to the specific structures in Fig. 8, to test the applicability of the Shard formula for these non-spherical core–shell NPs.

Shard formula

Shard proposed an empirical formula[26] for calculating the shell thickness of spherical core–shell NPs from the ratio of the XPS peak intensities of the core and shell elements. Implicit assumptions made for the formula are that the photoelectrons travel in straight lines in NPs and the photoelectron signal intensity decays exponentially with the distance travelled, where the decay rate is related to the photoelectron energy and the kind of material travelled in. Before presenting the Shard formula, an equation describing the relationship between the XPS signal intensity ratio (defined as A in eqn (11)) of overlayer and substrate and the related parameters, *i.e.* B, C, T, R (B and C are defined in eqn (12) and (13), T is the thickness of overlayer and R is the radius of core), has been proposed at first.[92] The relationship can be employed in an iterative manner to determine the overlayer thickness for NPs of known radius. In order to derive a simple and direct formula for converting XPS data to the thickness of the

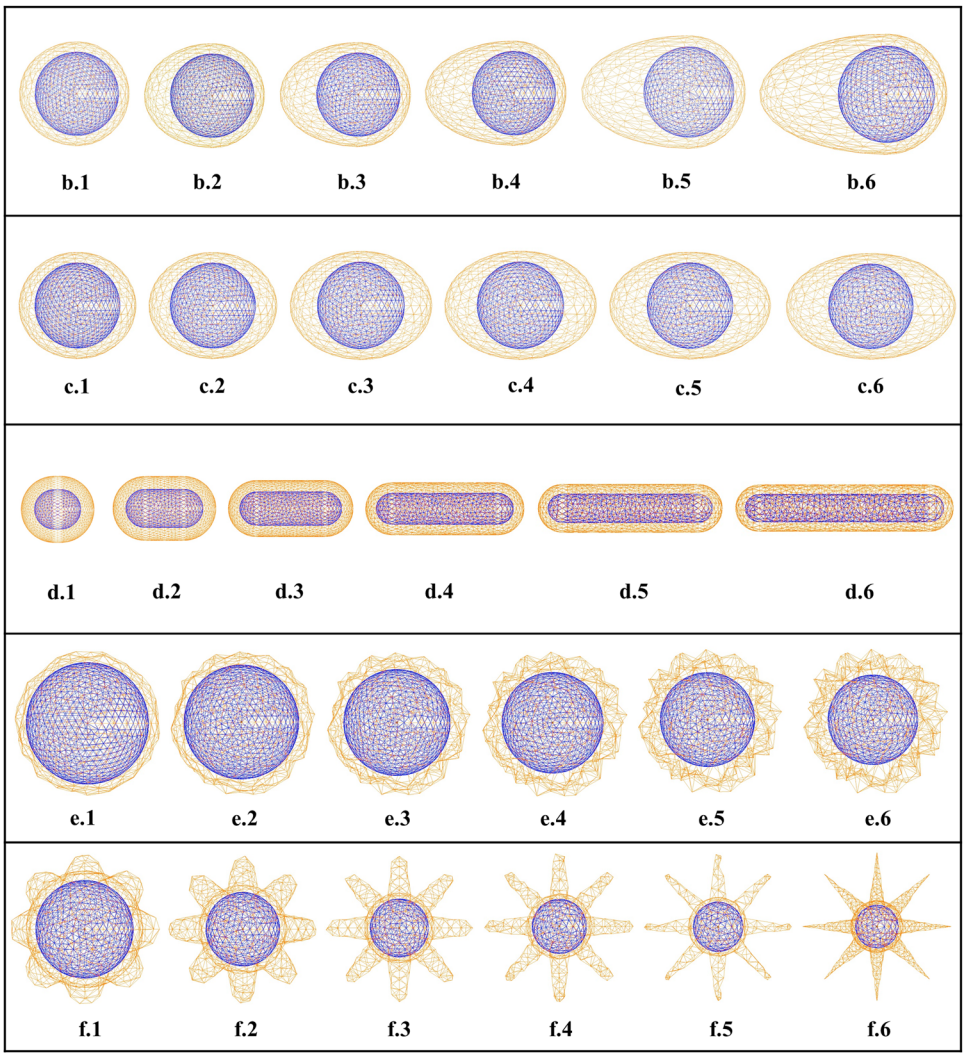

Fig. 8 Schematic of the considered core–shell NPs with various degrees of deformation: (b.1–b.6) egg, (c.1–c.6) ellipsoid, (d.1–d.6) rod, (e.1–e.6) rough-surface, (f.1–f.6) star.

overlayer instead of iterative calculation, the methodology used was to mix the formulae for extreme cases (*i.e.* for $R \to 0, R \to \infty$ *etc.*) by using weighting factors and adjusting the relevant parameters according to 6000 numerical calculations data. Before investigating NPs, a formula for predicting the thickness of the planar overlayer was first derived based on the iterative equation proposed by Cumpson.[93] Accordingly, the formula for the core radius $R \to \infty$ was derived by retaining the form of a planar case and optimizing the parameters. By combining the formula for infinitesimally small particles, the Shard formula for core–shell NPs with finite value R has then been obtained and the parameters are optimized by comparing the numerically calculated values.

The Shard formula is given as follows:

$$T_S = \frac{\left[0.74A^{3.6}\ln(A)B^{-0.9} + 4.2AB^{-0.41}\right]R}{(R+\alpha)(A^{3.6}+8.9)} + \frac{\beta R\left[(ABC+1)^{1/3}-1\right]}{1+\beta}; \quad (8)$$

$$\alpha = 1.8/(A^{0.1}B^{0.5}C^{0.4}); \quad (9)$$

$$\beta = 0.13\alpha^{2.5}/R^{1.5}; \quad (10)$$

$$A = I_1 I_2^{\infty}/I_1^{\infty} I_2; \quad (11)$$

$$B = L_{1,a}/L_{2,a}; \quad (12)$$

$$C = L_{1,a}/L_{1,b}, \quad (13)$$

where I_1 is the intensity of detected photoelectrons emitted from the shell, and I_2 is the intensity of detected photoelectrons emitted from the core. I_1^{∞} is the intensity of detected photoelectrons emitted from a semi-infinite bulk sample of shell material, and I_2^{∞} is the intensity of detected photoelectrons emitted from a semi-infinite bulk sample of core material. The geometries of X-ray incidence and photoelectrons detection are the same for a semi-infinite bulk sample system and core–shell sample system. $L_{i,j}$ is the electron attenuation length (EAL) of the photoelectrons that arise from material i and travel through material j; where $i = 1$ represents the shell material and $i = 2$

represents the core material; $j = a$ represents the shell material and $j = b$ represents the core material. All of the lengths in this formula are in units of $L_{1,a}$, and thus they are dimensionless quantities. For example, the radius R in the Shard formula in the present work denotes the ratio of the core radius to $L_{1,a}$. Likewise, the shell thickness T_S, where the subscript "S" represents the original Shard formulation for a spherical NP, is also represented in the unit of $L_{1,a}$.

The present work considers C-core/Au-shell NPs, in analogue to Powell *et al.*,[28] where the signals are C 1s and Au $4f_{7/2}$ photoelectrons. The relevant EALs can be estimated either from the NIST database[85] or from predictive formula.[94–96] Here $L_{1,a} = 1.29$ nm, $L_{2,a} = 1.14$ nm, $L_{1,b} = 3.32$ nm. Values of I_1^∞ and I_2^∞ are derived from our CTMC simulation of semi-infinite bulk materials.

Results and discussions

Non-spherical core–shell NPs

Fig. 9 illustrates the geometrical configuration of the exciting source, Al Kα X-ray, and the detector, where T represents the thickness of shell and D the diameter of core. For non-spherical NPs, whose equivalent radius and equivalent thickness will be defined later, there will be an effect of X-ray incident direction. In this case the geometry of the angle between the direction of X-ray and the electron detector is still set as fixed while the orientation of the detector (or equivalently the incident X-ray direction onto the NP) is changed over the whole solid angles of space.

Before considering non-spherical core–shell NPs, we first applied Shard formula on spherical core–shell NPs using our CTMC method. Our simulation results presented in Appendix II are almost the same as that of Powell *et al.*,[27] confirming the accuracy of the present Monte Carlo method. For the non-spherical core–shell NPs, *e.g.* the five different types shown in Fig. 7, the measurement of the shell thickness has always been difficult. We at first applied directly the Shard formula to these specific shapes to derive the estimated T_S; we then found an obvious deviation of the obtained thickness values from the actual values as represented by the volume equivalent thickness.

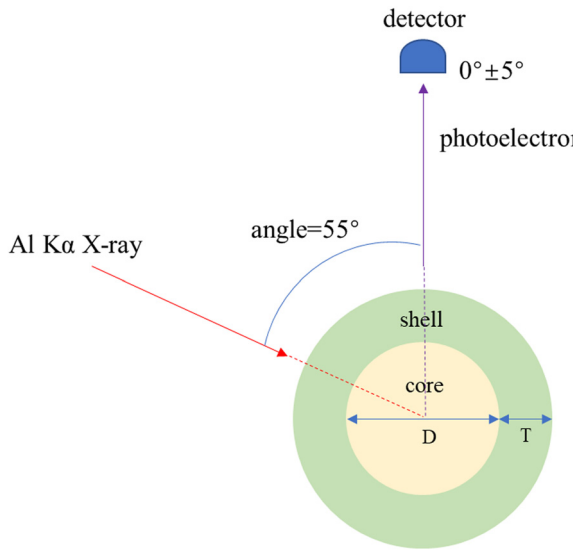

Fig. 9 Geometric conditions of XPS. The X-rays is incident at an angle of 55° with respect to the axis of the detector, and the collection range of the detector is less than 5°.

For the inhomogeneous shell thickness of irregularly shaped core–shell NPs, one needs to define an equivalent thickness for the representation of an average value of the uneven thickness. In the present work we used a volume equivalent quantity, which refers to the fact that a non-spherical NP is equivalent to a sphere of the same volume. Hence, the radius of the sphere is a proxy for the equivalent radius estimated from the realistic volume by

$$V_{c-s} = 4\pi R_{c-s}^3/3; \quad (14)$$

$$V_c = 4\pi R_c^3/3, \quad (15)$$

where V_{c-s} and V_c are respectively the volumes of a core–shell NP and of the core, and R_{c-s} and R_c are the equivalent sphere radiuses of the core–shell NP and of the core. Hence, the volume equivalent thickness of the shell is given by,

$$T = R_{c-s} - R_c; \quad (16)$$

For the estimation of the measurement error of the Shard formula, a relative error between the predicted shell thickness and the real thickness is defined by,

$$\Delta T_S = (T_S - T)/T; \quad (17)$$

We have performed Monte Carlo simulations for XPS signal emission from the five non-spherical NPs shown in Fig. 7 and 8 by changing the shape ratio of the core–shell NPs, such that the NPs gradually deformed from an ideal spherical core–shell NPs to the core–shell NPs with various distinct shape characteristics. Then we have estimated the shell thickness with the Shard formula where the core radius R is replaced by the equivalent sphere radius of core R_c for the rod shape. Fig. 10 compares the Shard formula predicted shell thickness with the volume equivalent shell thickness. It can be seen from Fig. 10(a), (b) and (d) that the closer a NP to a spherical shape, the higher accuracy of the shell thickness prediction of the Shard formula is; the accuracy gradually decreases with the deformation degree. For the rod NPs, the relative error can be as high as 70%, as shown by Fig. 10(c) and (f), which is undoubtedly related to the large deformation of the rod shape away from the sphere in the longitudinal direction while the ratio of the core–shell cross-sectional radius is kept the same. Regarding star shaped core–shell NPs in Fig. 10(e), the structure is much more complex than a sphere. Many parameters, like the waist and length of a star's arm, and the relative size of the arm and center ball, can influence the results.

Extended shard formula

Because of the various shapes and sizes of NPs, it is difficult to obtain a general formula for the shell thickness prediction in

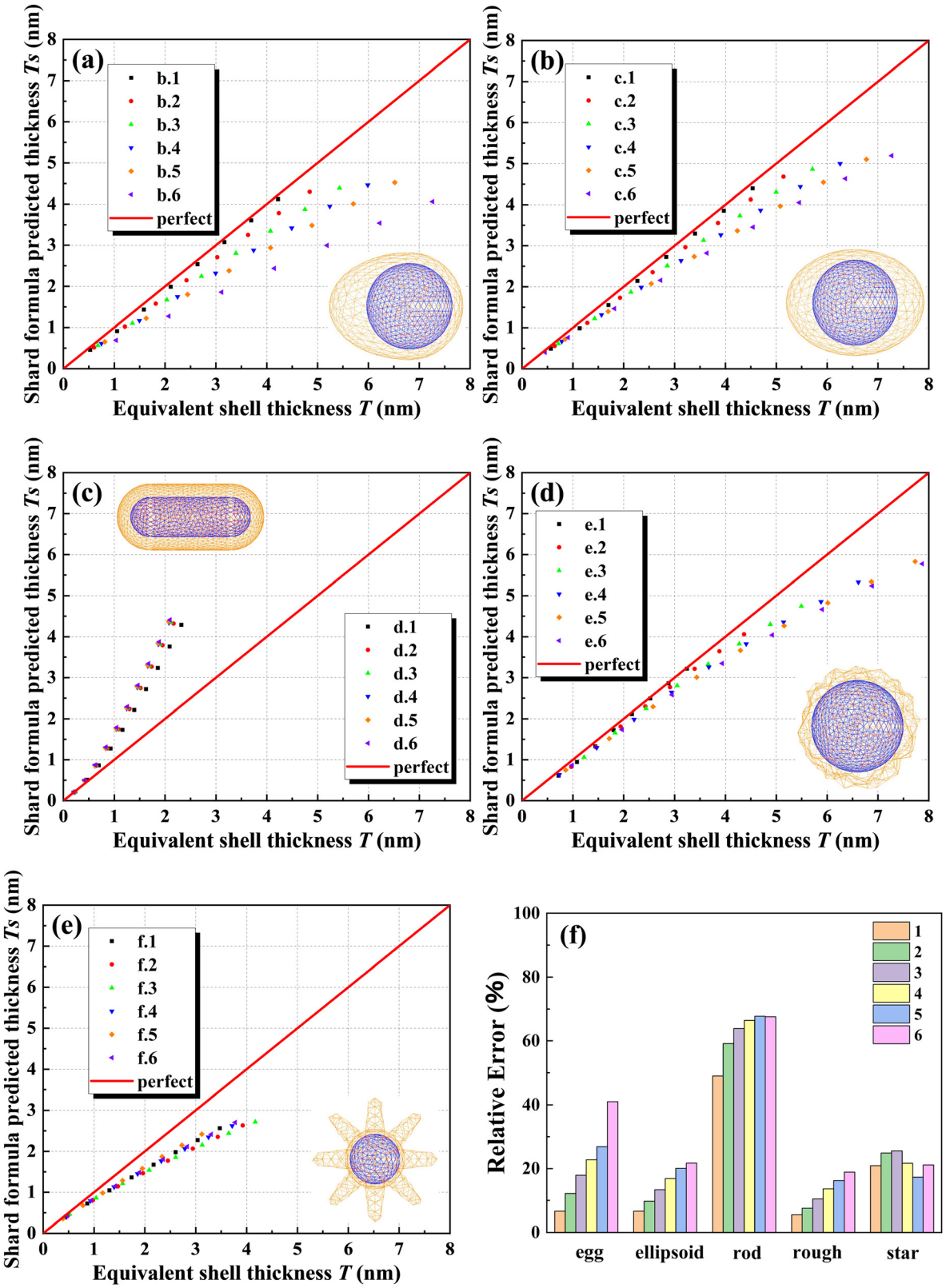

Fig. 10 Comparison between the Shard formula predicted shell thickness by eqn (8)–(13) and the volume equivalent shell thickness given by eqn (14)–(16) made on the Monte Carlo simulated XPS signals emitted from five shapes of core–shell NPs: (a) egg, (b) ellipsoid, (c) rod, (d) rough surface and (e) star. (f) Relative errors of the estimated shell thicknesses where the numerals for the color bar represent the deformation degree as shown in Fig. 8.

this context. Therefore, specific corrections to the Shard formula are made for the specific shapes considered. One may note from Fig. 10 that the output of the Shard formula, T_s, has approximately a linear relationship with the actual shell thickness, T. For a specific shape, we have obtained an extended Shard formula,

$$T_{ES} = \frac{\left[0.74A^{3.6}\ln(A)B^{-0.9} + 4.2AB^{-0.41}\right]RL_{1,a}}{(R+\alpha)(A^{3.6}+8.9)} + \beta R\left[(ABC+1)^{1/3}-1\right]L_{1,a} - b(1+\beta)}{(1+\beta)k}, \quad (18)$$

where two parameters for each type of core–shell NPs, k and b, represent the slope and intercept for linear fitting. T_{ES} is the shell thickness, where the subscript "ES" represents the extended Shard formulation for a non-spherical NP, which is represented in the unit of $L_{1,a}$. For $k = 1$ and $b = 0$, eqn (18) is equivalent to the Shard formula. The derived values of k and b from linear fitting are given in Tables 1–5, corresponding to each shape in Fig. 8.

Table 1 List of the parameters k and b in the extended Shard formula for egg-shaped NPs and the corresponding relative errors

	b.1	*b*.2	*b*.3	*b*.4	*b*.5	*b*.6
k	1.0053	0.9011	0.8099	0.7383	0.6810	0.5368
b	−0.1201	−0.0424	0.0257	0.0822	0.1297	0.1734
ΔT_S (%)	6.62	12.20	17.90	22.75	26.86	40.98
ΔT_{ES} (%)	1.97	1.11	0.88	1.25	1.50	1.75

Table 2 List of the parameters k and b in the extended Shard formula of ellipsoid-shaped NPs and the corresponding relative errors

	c.1	*c*.2	*c*.3	*c*.4	*c*.5	*c*.6
k	0.9962	0.9263	0.8563	0.7944	0.7415	0.7059
b	−0.1109	−0.0438	0.0301	0.0998	0.1631	0.1701
ΔT_S (%)	6.62	9.76	13.36	16.85	20.06	21.70
ΔT_{ES} (%)	1.67	0.96	1.51	2.24	2.77	5.34

Table 3 List of the parameters k and b in the extended Shard formula of rod-shaped NPs and the corresponding relative errors

	d.1	*d*.2	*d*.3	*d*.4	*d*.5	*d*.6
k	1.9848	2.1517	2.2271	2.2671	2.2836	2.2815
b	−0.4513	−0.4706	−0.4785	−0.4803	−0.4865	−0.4861
ΔT_S (%)	48.95	59.15	63.89	66.40	67.74	67.55
ΔT_{ES} (%)	7.70	7.58	7.49	7.46	7.30	7.36

Table 4 List of the parameters k and b in the extended Shard formula of rough-surface NPs and the corresponding relative errors

	e.1	*e*.2	*e*.3	*e*.4	*e*.5	*e*.6
k	1.0481	0.9563	0.8636	0.8021	0.7394	0.6843
b	−0.1634	−0.0613	0.0970	0.1825	0.3233	0.4688
ΔT_S (%)	5.49	7.55	10.47	13.62	16.27	18.90
ΔT_{ES} (%)	0.96	1.53	2.51	5.29	6.95	8.36

Fig. 11–15 show comparisons between the Shard formula and the extended Shard formula predicted shell thickness and the volume equivalent shell thickness for the egg-, ellipsoid-, rod-, rough-surface, and star-shaped core–shell NPs. Regarding each shape of core–shell NPs, Tables 1–5 indicate the values of the parameters, k and b. The corresponding relative error,

$$\Delta T_{ES} = (T_{ES} - T)/T; \quad (19)$$

has been greatly reduced to less than 10% for all of the various shapes of NPs considered in this work, which indicates that the extended Shard formula would be effective for predicting the shell thickness of core–shell NPs.

For spherical core–shell NPs, the results of shell thickness determination from our Monte Carlo simulated XPS signals are close to those of Powell *et al.*[27] and Shard[26] by using SESSA simulations, verifying that the Shard formula is universal for typical spherical core–shell NPs. In the present work although we only considered the C-core/Au-shell NPs, the generality of the extended Shard formula is also expected to be suitable for other elements in various core/shell architectures as in previous work.[27,28]

Summary

The Monte Carlo method has proven to be a valuable tool for simulating XPS signals for core–shell NPs with various geometrical morphologies. However, accurately determining the shell thickness of irregular-shaped core–shell NPs has been a challenge in previous research. In this study, we have addressed this challenge by providing an extended Shard formula that allows for quick and convenient measurements of shell thickness. Our results indicate that the relative error of the predicted shell thickness using the extended Shard formula is within 10% for the five irregular-shaped core–shell NPs investigated. Further studies could consider more shapes to establish a reference database.

The XPS method for determining shell thicknesses of core–shell NPs is a powerful tool that has numerous applications in both laboratory research and industry. For example, it can be used to regulate the size of core–shell quantum dots. One advantage of XPS over other methods, such as TEM, is its ability to quickly measure a large number of samples.

Table 5 List of the parameters k and b in the extended Shard formula of star-shaped NPs and the corresponding relative errors

	f.1	*f*.2	*f*.3	*f*.4	*f*.5	*f*.6
k	0.7157	0.6350	0.6121	0.6742	0.7559	0.6866
b	0.1032	0.1818	0.22050	0.1625	0.0888	0.1540
ΔT_S (%)	20.89	24.85	25.56	21.67	17.28	21.15
ΔT_{ES} (%)	1.86	3.71	4.65	3.60	1.98	3.24

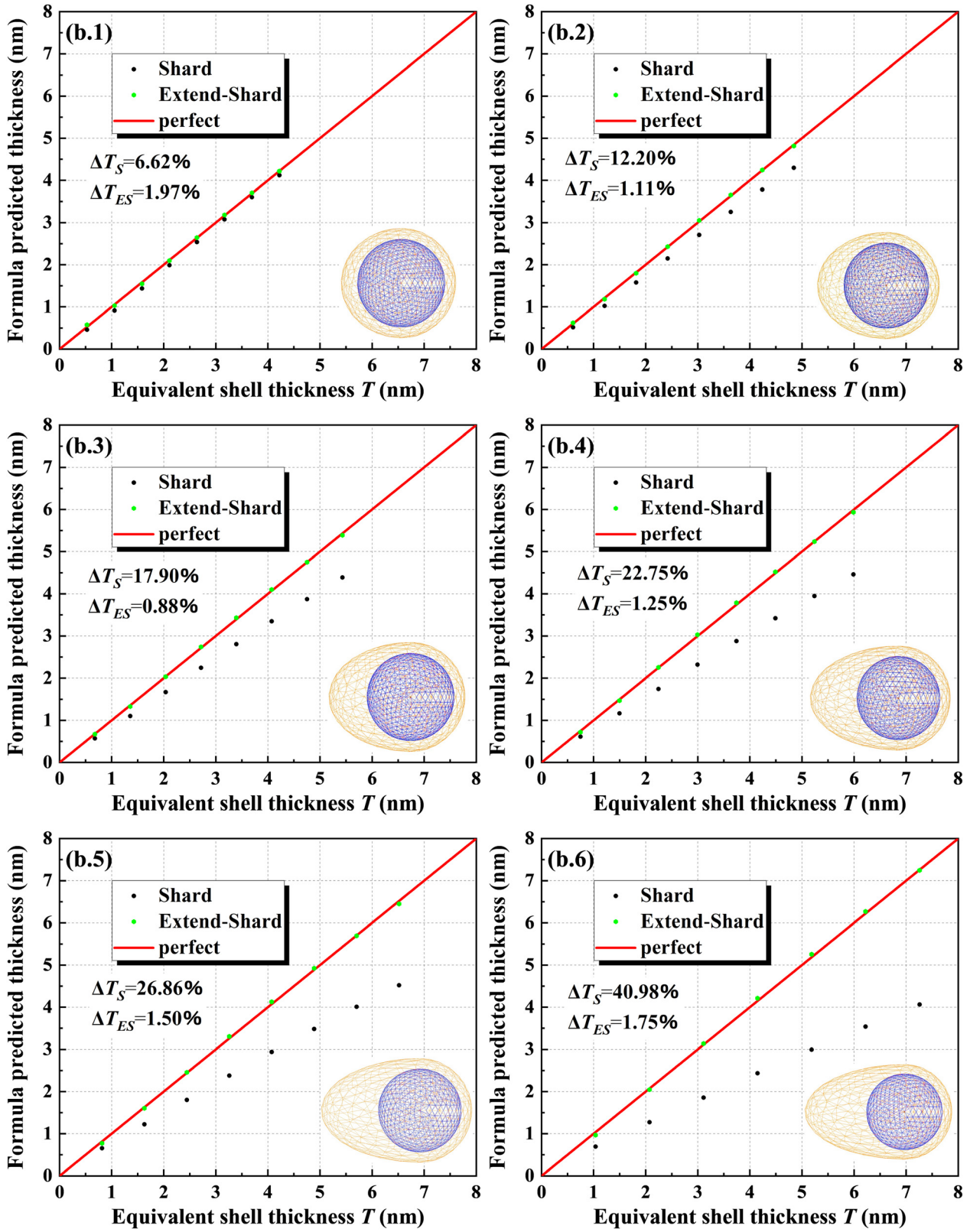

Fig. 11 Comparison between the Shard formula (eqn (8)–(13)) & the extended Shard formula (eqn (18)) predicted shell thickness and the volume equivalent shell thickness given by eqn (14)–(16) for the egg-shaped core–shell NPs. The black dots are the results of the Shard formula, and the green dots are the results of the extended Shard formula. The red line corresponds to the ideal estimation. The six graphs correspond to the egg-shaped core–shell NPs in Fig. 8(b.1)–(b.6).

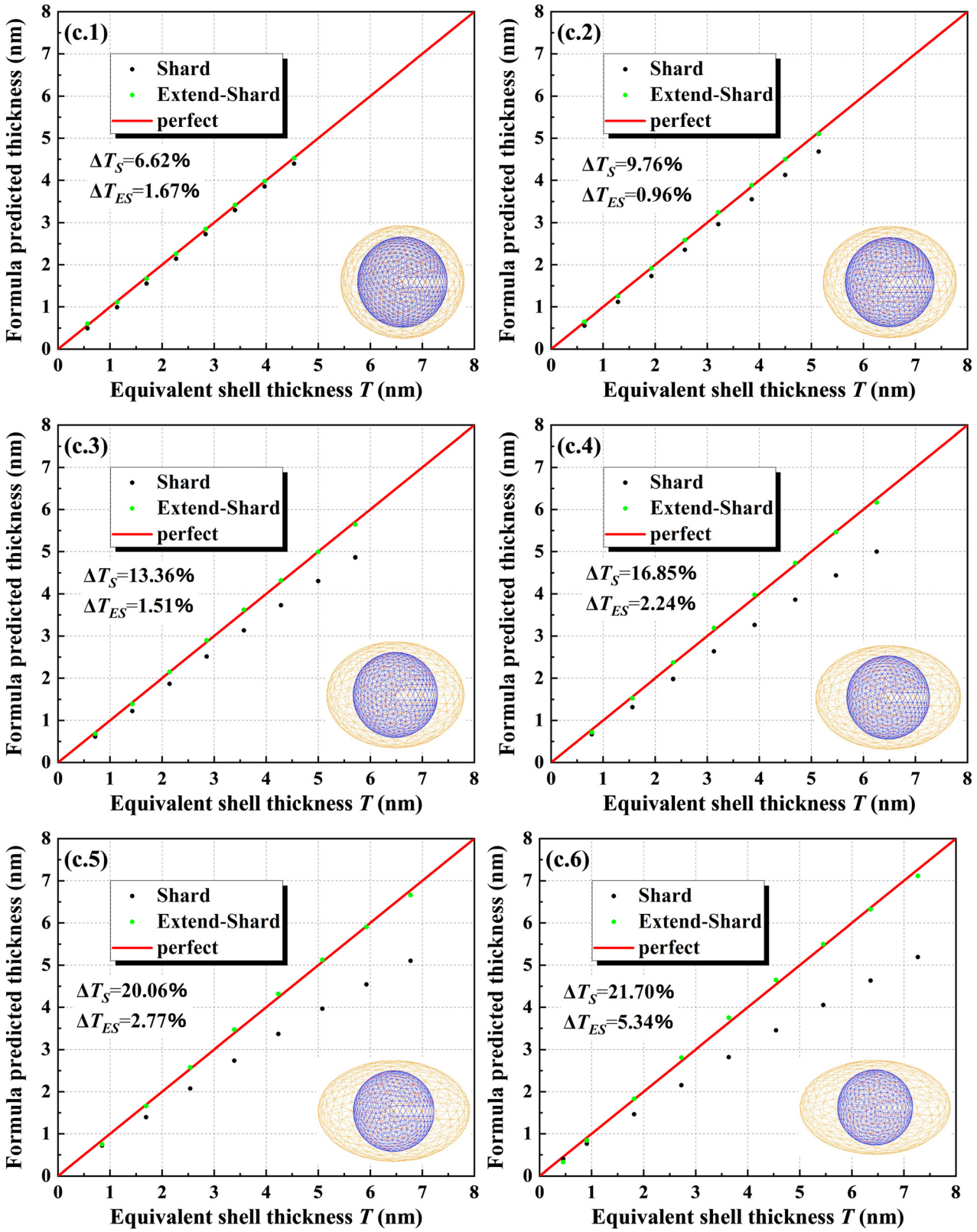

Fig. 12 Comparison between the Shard formula (eqn (8)–(13)) & the extended Shard formula (eqn (18)) predicted shell thickness and the volume equivalent shell thickness given by eqn (14)–(16) for the ellipsoid-shaped core–shell NPs. The black dots are the results of the Shard formula, and the green dots are the results of the extended Shard formula. The red line corresponds to the ideal estimation. The six graphs correspond to the ellipsoid-shaped core–shell NPs in Fig. 8(c.1)–(c.6).

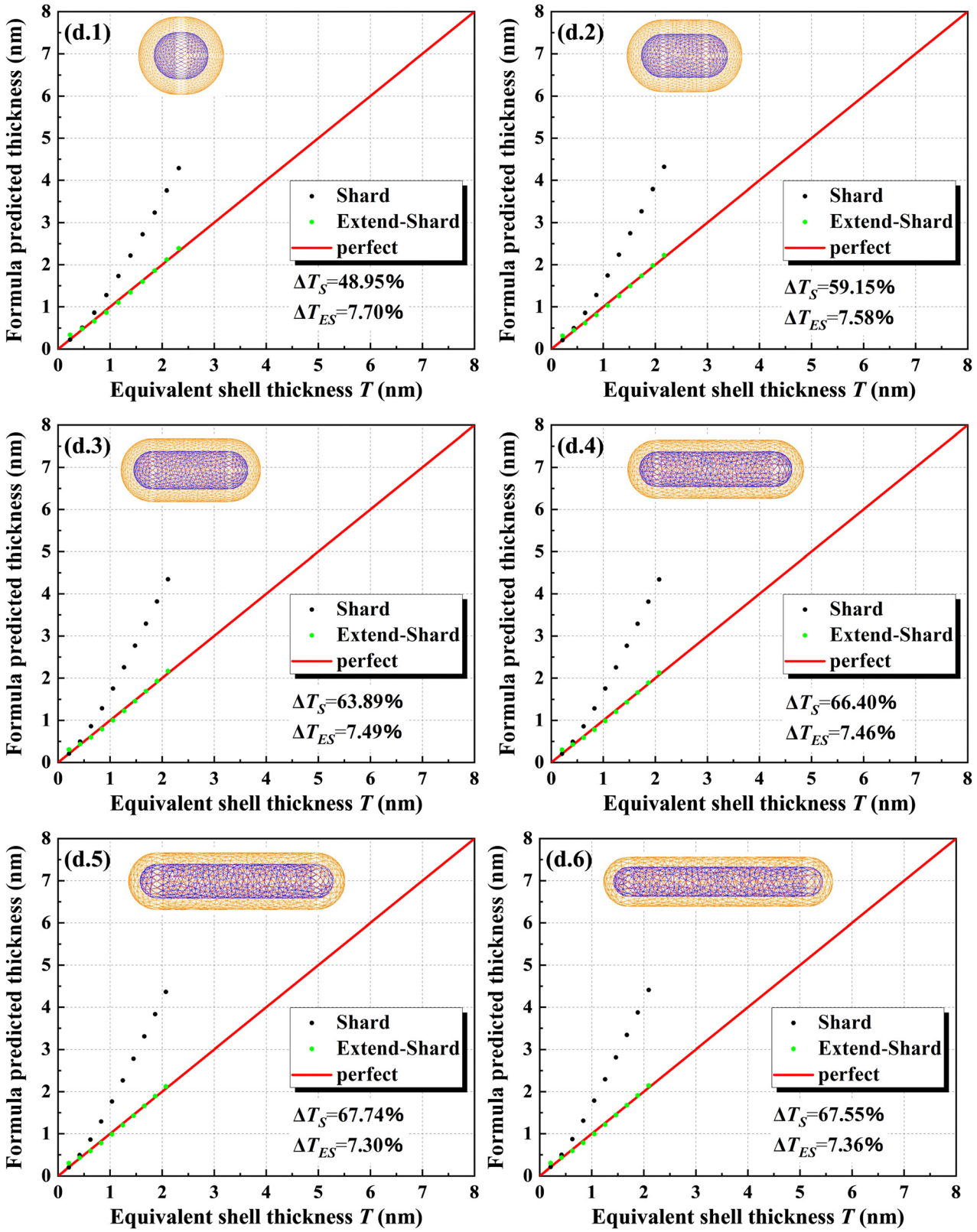

Fig. 13 Comparison between the Shard formula (eqn (8)–(13)) & the extended Shard formula (eqn (18)) predicted shell thickness and the volume equivalent shell thickness given by eqn (14)–(16) for the rod-shaped core–shell NPs. The black dots are the results of the Shard formula, and the green dots are the results of the extended Shard formula. The red line corresponds to the ideal estimation. The six graphs correspond to the rod-shaped core–shell NPs in Fig. 8(d.1)–(d.6).

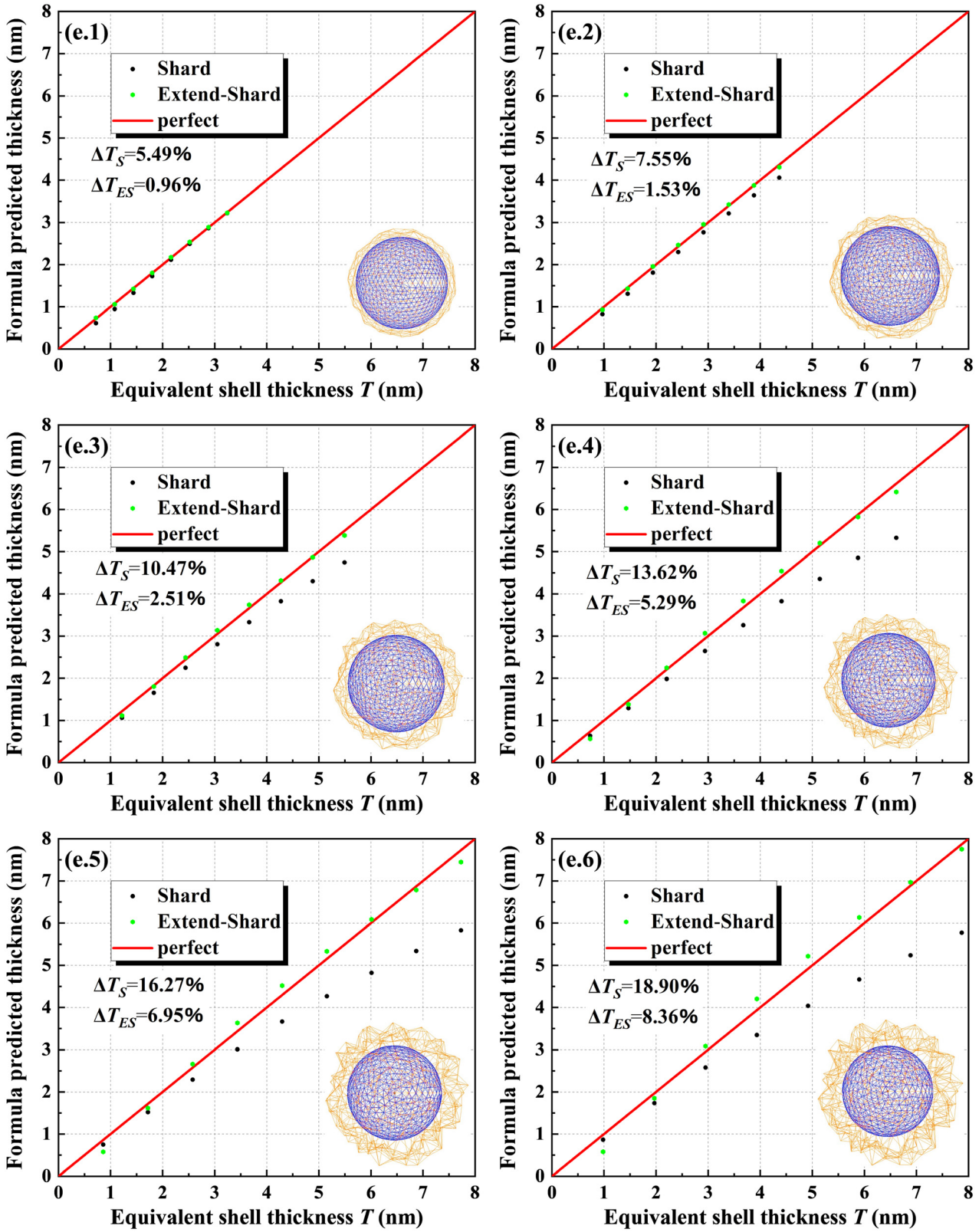

Fig. 14 Comparison between the Shard formula (eqn (8)–(13)) & the extended Shard formula (eqn (18)) predicted shell thickness and the volume equivalent shell thickness given by eqn (14)–(16) for the rough surface core–shell NPs. The black dots are the results of the Shard formula, and the green dots are the results of the extended Shard formula. The red line corresponds to the ideal estimation. The six graphs correspond to the rough surface core–shell NPs in Fig. 8(e.1)–(e.6).

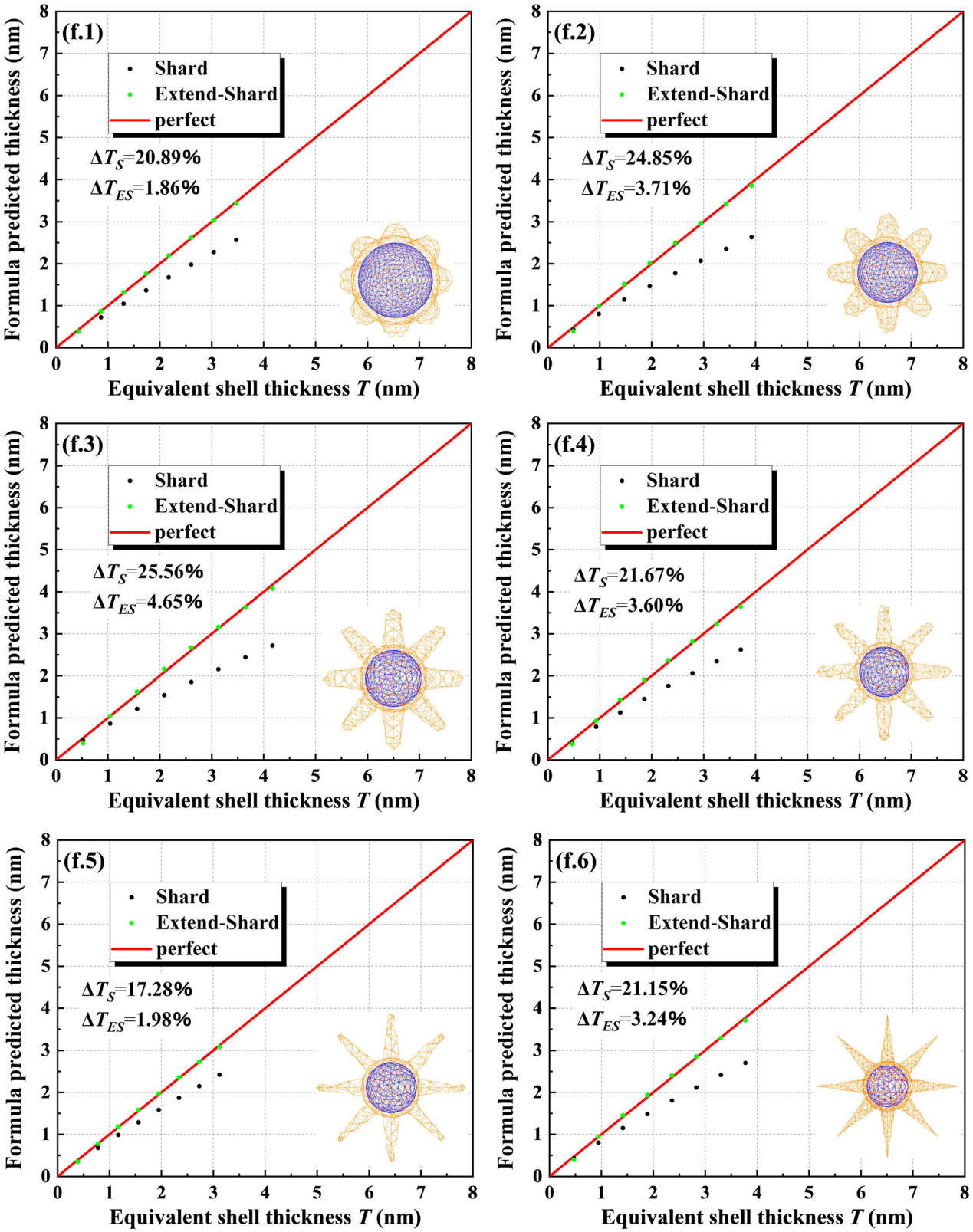

Fig. 15 Comparison between the Shard formula (eqn (8)–(13)) & the extended Shard formula (eqn (18)) predicted shell thickness and the volume equivalent shell thickness given by eqn (14)–(16) for the star-shaped core–shell NPs. The black dots are the results of the Shard formula, and the green dots are the results of the extended Shard formula. The red line corresponds to the ideal estimation. The six graphs correspond to the star-shaped core–shell NPs in Fig. 8(f.1)–(f.6).

While our study has focused on the intensity of photoelectrons, the shape of the peak may also provide useful information that could be explored in future work. Overall, our findings demonstrate the potential of XPS as a valuable technique for characterizing core–shell NPs and highlight the importance of developing accurate and efficient methods for determining shell thickness in irregular-shaped NPs.

Conflicts of interest

There are no conflicts to declare.

Acknowledgements

This work was supported by the Chinese Education Ministry through ''111 Project 2.0'' (BP0719016), the The Kurata Grants from The Hitachi Global Foundation and from The Iketani Science & Technology Foundation. We also thank Dr H. M. Li and the supercomputing center of USTC for parallel computing support.

References

1 C. F. Jones, D. G. Castner and D. W. Grainger, *Handbook of Immunological Properties of Engineered Nanomaterials*, World Scientific, 2013, pp. 117–149.
2 A. S. Karakoti, L. L. Hench and S. Seal, *JOM*, 2006, **58**, 77–82.
3 M. Khatami, H. Q. Alijani, M. S. Nejad and R. S. Varma, *Appl. Sci.*, 2018, **8**, 411.
4 A. Henglein, *Chem. Rev.*, 1989, **89**, 1861–1873.
5 L. Spanhel, H. Weller and A. Henglein, *J. Am. Chem. Soc.*, 1987, **109**, 6632–6635.
6 H. C. Youn, S. Baral and J. H. Fendler, *J. Phys. Chem.*, 1988, **92**, 6320–6327.
7 C. F. Hoener, K. A. Allan, A. J. Bard, A. Campion, M. A. Fox, T. E. Mallouk, S. E. Webber and J. M. White, *J. Phys. Chem.*, 1992, **96**, 3812–3817.
8 I. Honma, T. Sano and H. Komiyama, *J. Phys. Chem.*, 1993, **97**, 6692–6695.
9 H. S. Zhou, H. Sasahara, I. Honma, H. Komiyama and J. W. Haus, *Chem. Mater.*, 1994, **6**, 1534–1541.
10 R. Ghosh Chaudhuri and S. Paria, *Chem. Rev.*, 2012, **112**, 2373–2433.
11 S. L. Maas, M. L. Broekman and J. D. Vrij, *Exosomes and Microvesicles*, Springer, 2017, pp. 21–33.
12 J. Grobelny, F. W. DelRio, N. Pradeep, D.-I. Kim, V. A. Hackley and R. F. Cook, *Characterization of Nanoparticles Intended for Drug Delivery*, Springer, 2011, pp. 71–82.
13 A. A. Dongargaonkar and J. D. Clogston, *Characterization of Nanoparticles Intended for Drug Delivery*, Springer, 2018, pp. 57–63.
14 P. Klapetek, M. Valtr, D. Nečas, O. Salyk and P. Dzik, *Nanoscale Res. Lett.*, 2011, **6**, 1–9.
15 A. G. Shard, *Characterization of Nanoparticles*, Elsevier, 2020, pp. 349–371.
16 J. C. Riviere and S. Myhra, *Handbook of Surface and Interface Analysis: Methods for Problem-Solving*, CRC Press, 2009.
17 A. Jablonski and C. J. Powell, *Surf. Sci. Rep.*, 2002, **47**, 33–91.
18 C. J. Powell and A. Jablonski, *J. Electron Spectrosc. Relat. Phenom.*, 2010, **178**, 331–346.
19 D. R. Baer and M. H. Engelhard, *J. Electron Spectrosc. Relat. Phenom.*, 2010, **178**, 415–432.
20 S. M. Davis, *J. Catal.*, 1989, **117**, 432–446.
21 R. Wojcieszak, M. Genet, P. Eloy, P. Ruiz and E. M. Gaigneaux, *J. Phys. Chem. C*, 2010, **114**, 16677–16684.
22 L. Coronel, J. Múnera, A. M. Tarditi, M. Moreno and L. M. Cornaglia, *Appl. Catal., B*, 2014, **160**, 254–266.
23 A. M. Tarditi, N. Barroso, A. E. Galetti, L. A. Arrúa, L. Cornaglia and M. C. Abello, *Surf. Interface Anal.*, 2014, **46**, 521–529.
24 M. Y. Smirnov, A. V. Kalinkin, A. V. Bukhtiyarov, I. P. Prosvirin and V. I. Bukhtiyarov, *J. Phys. Chem. C*, 2016, **120**, 10419–10426.
25 D.-Q. Yang, M. Meunier and E. Sacher, *Appl. Surf. Sci.*, 2001, **173**, 134–139.
26 A. G. Shard, *J. Phys. Chem. C*, 2012, **116**, 16806–16813.
27 C. J. Powell, W. Werner, A. Shard and D. G. Castner, *J. Phys. Chem. C*, 2016, **120**, 22730–22738.
28 C. J. Powell, W. S. M. Werner, H. Kalbe, A. G. Shard and D. G. Castner, *J. Phys. Chem. C*, 2018, **122**, 4073–4082.
29 M. Gao, L. Zhu, W. L. Ong, J. Wang and G. W. Ho, *Catal. Sci. Technol.*, 2015, **5**, 4703–4726.
30 V. Chiozzi and F. Rossi, *Nanoscale Adv.*, 2020, **2**, 5090–5105.
31 S. Ichimura, Z. J. Ding and R. Shimizu, *Surf. Interface Anal.*, 1988, **13**, 149–159.
32 R. Shimizu and Z. J. Ding, *Rep. Prog. Phys.*, 1992, **55**, 487.
33 D. C. Joy, *Monte Carlo Modeling for Electron Microscopy and Microanalysis*, Oxford University Press, 1995.
34 Z. J. Ding and R. Shimizu, *Scanning*, 1996, **18**, 92–113.
35 M. Dapor, *Transport of Energetic Electrons in Solids: Computer Simulation with Applications to Materials Analysis and Characterization*, Springer, 2016.
36 Z. J. Ding, C. Li, B. Da and J. W. Liu, *Sci. Technol. Adv. Mater.*, 2021, **22**, 932–971.
37 Z. J. Ding, T. Nagatomi, R. Shimizu and K. Goto, *Surf. Sci.*, 1995, **336**, 397–403.
38 Z. J. Ding, X. D. Tang and R. Shimizu, *J. Appl. Phys.*, 2001, **89**, 718–726.
39 Z. J. Ding, X. D. Tang and H. M. Li, *Int. J. Mod. Phys. B*, 2002, **16**, 4405–4412.
40 Z. J. Ding, H. M. Li, X. D. Tang and R. Shimizu, *Appl. Phys. A*, 2004, **78**, 585–587.
41 Z. J. Ding, H. M. Li, K. Goto, Y. Z. Jiang and R. Shimizu, *J. Appl. Phys.*, 2004, **96**, 4598–4606.
42 C. Li, B. Da and Z. J. Ding, *Appl. Surf. Sci.*, 2020, **504**, 144138.
43 Z. J. Ding and R. Shimizu, *J. Microscopy*, 1989, **154**, 193–207.
44 H. M. Li and Z. J. Ding, *Scanning*, 2005, **27**, 254–267.
45 Y. T. Yue, H. M. Li and Z. J. Ding, *J. Phys. D*, 2005, **38**, 1966.
46 Z. J. Ding and H. M. Li, *Surf. Interface Anal.*, 2005, **37**, 912–918.
47 Y. G. Li, S. F. Mao, H. M. Li, S. M. Xiao and Z. J. Ding, *J. Appl. Phys.*, 2008, **104**, 064901.

48 S. F. Mao and Z. J. Ding, *Surf. Interface Anal.*, 2010, **42**, 1096–1099.
49 P. Zhang, H. Y. Wang, Y. G. Li, S. F. Mao and Z. J. Ding, *Scanning*, 2012, **34**, 145–150.
50 Y. G. Li, P. Zhang and Z. J. Ding, *Scanning*, 2013, **35**, 127–139.
51 Y. B. Zou, M. S. S. Khan, H. M. Li, Y. G. Li, W. Li, S. T. Gao, L. S. Liu and Z. J. Ding, *Measurement*, 2018, **123**, 150–162.
52 M. S. S. Khan, L. H. Yang, X. Deng, S. F. Mao, Y. B. Zou, Y. G. Li, H. M. Li and Z. J. Ding, *J. Phys. D*, 2021, **54**, 445301.
53 Z. J. Ding, R. Shimizu, T. Sekine and Y. Sakai, *Appl. Surf. Sci.*, 1988, **33**, 99–106.
54 Y. G. Li, Z. J. Ding and Z. M. Zhang, *J. Appl. Phys.*, 2009, **106**, 024316.
55 N. Cao, B. Da, Y. Ming, S. F. Mao, K. Goto and Z. J. Ding, *Surf. Interface Anal.*, 2015, **47**, 113–119.
56 D. S. You, H. M. Li and Z. J. Ding, *J. Electron Spectrosc. Relat. Phenom.*, 2018, **222**, 156–161.
57 B. Da, S. F. Mao and Y. Sun, *e-J. Surf. Sci. Nanotechnol.*, 2012, **10**, 441–446.
58 B. Da, Y. Sun, S. F. Mao, Z. M. Zhang, H. Jin, H. Yoshikawa, S. Tanuma and Z. J. Ding, *J. Appl. Phys.*, 2013, **113**, 214303.
59 H. Xu, B. Da, J. Tóth, K. Tőkési and Z. J. Ding, *Phys. Rev. B*, 2017, **95**, 195417.
60 H. Xu, L. H. Yang, B. Da, J. Tóth, K. Tőkési and Z. J. Ding, *Nucl. Instrum. Methods Phys. Res., Sect. B*, 2017, **406**, 475–481.
61 H. Xu, L. H. Yang, J. Tóth, K. Tőkési, B. Da and Z. J. Ding, *J. Appl. Phys.*, 2018, **123**, 043306.
62 L. H. Yang, M. Menyhárd, A. Sulyok, K. Tőkési and Z. J. Ding, *Appl. Surf. Sci.*, 2018, **456**, 999–1003.
63 L. H. Yang, K. Tőkési, J. Tóth, B. Da, H. M. Li and Z. J. Ding, *Phys. Rev. B*, 2019, **100**, 245209.
64 L. H. Yang, J. M. Gong, A. Sulyok, M. Menyhárd, G. Sáfrán, K. Tőkési, B. Da and Z. J. Ding, *Phys. Chem. Chem. Phys.*, 2021, **23**, 25335–25346.
65 A. Hussain, L. H. Yang, S. F. Mao, B. Da, K. Tőkési and Z. J. Ding, *Nuclear Mater. Energy*, 2021, **26**, 100862.
66 B. Da, Z. Y. Li, H. C. Chang, S. F. Mao and Z. J. Ding, *J. Appl. Phys.*, 2014, **116**, 124307.
67 B. Da, L. H. Yang, J. W. Liu, Y. G. Li, S. F. Mao and Z. J. Ding, *Surf. Interface Anal.*, 2020, **52**, 742–754.
68 B. Da, J. W. Liu, M. Yamamoto, Y. Ueda, K. Watanabe, N. T. Cuong, S. Li, K. Tsukagoshi, H. Yoshikawa and H. Iwai, *Nat. Commun.*, 2017, **8**, 1–9.
69 N. W. M. Ritchie, *Surf. Interface Anal.*, 2005, **37**, 1006–1011.
70 B. Da, S. F. Mao, G. H. Zhang, X. P. Wang and Z. J. Ding, *Surf. Interface Anal.*, 2012, **44**, 647–652.
71 B. Da, S. F. Mao, G. H. Zhang, X. P. Wang and Z. J. Ding, *J. Appl. Phys.*, 2012, **112**, 034310.
72 X. Ding, B. Da, J. B. Gong, S. F. Mao, H. M. Li and Z. J. Ding, *Surf. Interface Anal.*, 2014, **46**, 489–496.
73 B. Da, K. Salma, H. Ji, S. F. Mao, G. H. Zhang, X. P. Wang and Z. J. Ding, *Appl. Surf. Sci.*, 2015, **356**, 142–149.
74 C. Li, S. F. Mao, Y. B. Zou, Y. G. Li, P. Zhang, H. M. Li and Z. J. Ding, *J. Phys. D*, 2018, **51**, 165301.
75 J. Almansa, F. Salvat-Pujol, G. Díaz-Londoño, A. Carnicer, A. M. Lallena and F. Salvat, *Comput. Phys. Commun.*, 2016, **199**, 102–113.
76 F. Salvat, J. M. Fernández-Varea and J. Sempau, *PENELOPE-2006: A Code System for Monte Carlo Simulation of Electron and Photon Transport, Workshop proceedings*, Nuclear Energy Agency, Organization for Economic Cooperation and Development, Barcelona, Spain, 2006.
77 F. Salvat, J. M. Fernández-Varea and J. Sempau, *PENELOPE-2008: A Code System for Monte Carlo Simulation of Electron and Photon Transport, Workshop proceedings*, Nuclear Energy Agency, Organization for Economic Cooperation and Development, Barcelona, Spain, 2008.
78 J. S. Villarrubia, A. Vladár, B. Ming, R. J. Kline, D. F. Sunday, J. Chawla and S. List, *Ultramicroscopy*, 2015, **154**, 15–28.
79 N. F. Mott, *Proc. R. Soc. London, Ser. A*, 1929, **124**, 425–442.
80 R. A. Bonham and T. G. Strand, *J. Chem. Phys.*, 1963, **39**, 2200–2204.
81 E. D. Palik, *Handbook of Optical Constants of Solids*, Academic Press, 1998.
82 D. R. Penn, *Phys. Rev. B: Condens. Matter Mater. Phys.*, 1987, **35**, 482.
83 S. F. Mao, Y. G. Li, R. G. Zeng and Z. J. Ding, *J. Appl. Phys.*, 2008, **104**, 114907.
84 H.-J. Hagemann, W. Gudat and C. Kunz, *JOSA*, 1975, **65**, 742–744.
85 C. Powell and A. Jablonski, *US Department of Commerce, National Institute of Standards and Technology*, 2011.
86 I. Band, Y. I. Kharitonov and M. Trzhaskovskaya, *At. Data Nucl. Data Tables*, 1979, **23**, 443–505.
87 C. Geuzaine and J. F. Remacle, *Int. J. Numer. Meth. Eng.*, 2009, **79**, 1309–1331.
88 N. Pazos-Pérez, B. Rodríguez-González, M. Hilgendorff, M. Giersig and L. M. Liz-Marzán, *J. Mater. Chem.*, 2010, **20**, 61–64.
89 S. Wang, R. F. Huo, R. Zhang, Y. C. Zheng, C. J. Li and L. Pan, *RSC Adv.*, 2018, **8**, 24866–24872.
90 **https://eusmi-h2020.eu/access/wp4/NSL-BIOMA**.
91 X. M. Zhang, S. S. Ye, X. Zhang and L. P. Wu, *J. Mater. Chem. C*, 2015, **3**, 2282–2290.
92 A. G. Shard, J. Wang and S. J. Spencer, *Surf. Interface Anal.*, 2009, **41**, 541–548.
93 P. J. Cumpson, *Surf. Interface Anal.*, 2000, **29**, 403–406.
94 A. Jablonski and C. Powell, *J. Vac. Sci. Technol., A*, 2009, **27**, 253–261.
95 M. Seah and I. Gilmore, *Surf. Interface Anal.*, 2001, **31**, 835–846.
96 A. Jablonski and C. Powell, *J. Electron Spectrosc. Relat. Phenom.*, 2015, **199**, 27–37.

